Structural and analytical characterization of Si_{1-x} Ge_x /Si heterostructures by Rutherford backscattering spectrometry and channeling, analytical electron microscopy and double crystal X-ray diffractometry

Aldo Armigliato([1]), Marco Servidori([1]), Franco Cembali([1]), Rita Fabbri([1]),
Rodolfo Rosa([1]), Franco Corticelli([1]), Donato Govoni([1]), Antonio V. Drigo([2]),
Massimo Mazzer([2]), Filippo Romanato([2]), Stefano Frabboni([3]), Roberto Balboni([3]),
Subramanian S.Iyer([4]) and Antonella Guerrieri([5])

([1]) CNR-Istituto LAMEL, via Castagnoli 1, 40126 Bologna, Italy
([2]) Dipartimento di Fisica and Unità GNSM-INFM, Università di Padova, via Marzolo 8, 35131 Padova, Italy
([3]) Dipartimento di Fisica, Univ. di Modena, via G. Campi 213/A, 41100 Modena, Italy
([4]) IBM Research Division T.J. Watson Res. Center, Yorktown Heights, PO Box 218, NY 10598, U.S.A.
([5]) Centro Nazionale per la Ricerca e lo Sviluppo dei Materiali (CNRSM) Via Marconi 147, 72023 Mesagne, Italy

Abstract. — Thin film $Si_{1-x}Ge_x$ alloys have been grown on silicon by molecular beam epitaxy with nominal composition, x, between 10 and 20 at %. These heterostructures have several applications in band-engineering and in the field of device structures. Film thicknesses, germanium atomic fractions and tetragonal distortion were determined by three different techniques, i.e. Rutherford Backscattering Spectrometry-Channeling, Analytical Electron Microscopy and Double Crystal X-ray Diffractometry. The good agreement found between the various analytical results demonstrates that each technique is capable of a high level of accuracy and consistency. These characterization methods are therefore powerful tools for the precise control of the epitaxial layer growth parameters for the fabbrication of different device structures.

1. Introduction.

Silicon-germanium alloys are presently receiving considerable attention due to the progress in the growth of strained coherent Si-Ge layers on silicon, which has made bandgap engineering possible in silicon technology. The feasibility of Si-Ge-based heterojunction bipolar transistors (HBTs) has been demonstrated few years ago [1]. Other device structures such as FETs and optoelectronics detectors have also been demonstrated.

Very recently HBTs have been realized with high transit frequencies up to 75 GHz [2] and

low base sheet resistivities down to 0.3 kohm/□ for a 50 nm thick base [3]. The thickness of the $Si_{1-x}Ge_x$ layer is an important device design parameter. The maximum thickness for pseudo-morphic growth ("critical thickness") of the alloy is strongly related to the Ge atomic fraction x. Moreover, the bandgap width of the alloy depends on the value of the lattice strain, which, in turn, considerably affects the transit time of the electrons in the base region. Therefore thickness, Ge concentration and lattice strain of the thin film Si-Ge alloys are parameters that must be accurately determined and controlled.

$Si_{1-x}Ge_x$ films grown on Si by Molecular Beam Epitaxy (MBE) have been analyzed by Rutherford Backscattering Spectrometry (RBS) and Channeling, Analytical Electron Microscopy (AEM) and Double Crystal X-ray Diffractometry (DCXD). In AEM, the Ge concentration have been determined by Energy Dispersive X-ray Spectrometry (EDS) and the lattice strain by Convergent Beam Electron Diffraction (CBED). The combined use of these three techniques allows us to critically discuss the accuracy of the procedures employed for the quantitative analyses.

2. Sample preparation.

$Si_{1-x}Ge_x$ alloys were grown by conventional solid source MBE. The details of the growth have been described in reference [4]. Briefly, Si and Ge are each evaporated from electron beam sources that are individually closed loop controlled. The substrate temperature is independently controlled, by radiant heating from behind the wafer. As it has been described alsewhere [15] the growth of abrupt Si/SiGe structures requires low temperatures. The films employed in this study were typically grown at 550°C at growth rates of about 0.5 nm/s. Prior to growth the Si(100) wafers were RCA cleaned and *in situ* cleaned at temperatures of about 900 °C for 20 minutes. This resulted in an atomically clean surface on which a thin (typically 100 nm) Si buffer was grown at 650 °C. The temperature was then ramped down and the SiGe layer was grown. Finally, a protective Si cap, either 5 or 100 nm thick was grown at 550 °C on the top of the heterostructures. The nominal Ge atomic fraction varied between 10 and 20 at %. The nominal features of the specimens investigated in this work are listed in table I.

Table I. — *Nominal layer thicknesses* (nm) *and* Ge *atomic fractions of the MBE grown samples.*

sample	cap thickness	alloy thickness	buffer thickness	Ge atomic fraction
#1	5	100	100	0.10
#2	100	100	100	0.15
#3	5	100	100	0.20
#4	100	100	100	0.20

3. Basic formulation of the strain related quantities.

Often in literature different symbols and different quantities are employed to describe the consequences of the lack of matching of the lattice parameters in the epitaxial growth of heterostructures. In particular, terms such as misfit, mismatch, distortion and strain are sometimes given

different meanings. For this reason, the basic formulation of these quantities is briefly reported in the following, giving particular emphasis to the analogies and differences between the quantities measured by the different techniques.

A crystalline alloy, having a bulk lattice parameter a_x (depending on the molar fraction, x, of the solute) grown on a substrate of lattice parameter a_0, is characterized by the misfit parameter

$$f = \frac{a_x - a_0}{a_0} \qquad (1)$$

Nevertheless, it is well known that for sufficiently small thicknesses, depending on the misfit value, the atoms of the growing layer can be forced to grow coherently with the underlying structure by the stress exerted by the surface interatomic potentials. The lattice of the epilayer will thus be strained and the relation between stress and strain can be found in the framework of the linear elasticity theory, which relates the stress to the strain tensor through the matrix of the elastic constants of the material. In the simple case of cubic lattices and (001) growth plane (as in our case) the tensor equation reduced to a simple vector equation whose components can be written as [6]

$$\begin{pmatrix} \sigma_1 \\ \sigma_2 \\ \sigma_3 \end{pmatrix} = \begin{pmatrix} c_{11} & c_{12} & c_{12} \\ c_{12} & c_{11} & c_{12} \\ c_{12} & c_{12} & c_{11} \end{pmatrix} \begin{pmatrix} \varepsilon_1 \\ \varepsilon_2 \\ \varepsilon_3 \end{pmatrix} \qquad (2)$$

where σ_i and ε_i are the components of stress and strain, respectively, and c_{11}, c_{12} are two of the three elastic (stiffness) constants. In the case of a thin film grown on a thick (semi-inifinite) substrate, the deformations described by equation (2) are limited to the film, while the subtrate will not be strained.

In the simple case of (001) growth we are considering, $\sigma_3 = 0$, as there is no force normal to the free surface. For symmetry reasons $\varepsilon_1 = \varepsilon_2 = \varepsilon_\parallel$ while $\varepsilon_3 = \varepsilon_\perp$, i.e. for a coherent growth there are only two components of the strain, respectively parallel and perpendicular to the growth plane: we are in presence of a simple biaxial strain field and the cubic lattice cell of the epilayer becomes tetragonally distorted.

The strain components are given by the relative difference of the actual and the bulk (free) lattice parameters:

$$\varepsilon_{\perp x} = \frac{a_{\perp x}}{a_x} - 1 \qquad (3a)$$

$$\varepsilon_{\parallel x} = \frac{a_{\parallel x}}{a_x} - 1 \qquad (3b)$$

The equilibrium equations in terms of the stress vector turn out to be

$$\frac{\partial \sigma_i}{\partial x_i} = 0 \qquad (4)$$

where $x_i (i = 1, 2, 3)$ are the cartesian coordinate along the lattice cell axes. As the growth plane is considered to be infinite in extension compared to the film thickness, the stress components can be chosen to be independent of both x_1 and x_2. As a consequence only the equation (4) with $i = 3$ is non-trivial and when combined with equation (2), gives:

$$2c_{12}\,\varepsilon_{\parallel x} + c_{11}\,\varepsilon_{\perp x} = \text{const} = 0 \qquad (5)$$

because of the boundary condition at the free surface. Thus the strain components are linked together by the Poisson's relation

$$\varepsilon_{\perp x} = -\alpha\,\varepsilon_{\parallel x} \qquad (6)$$

where

$$\alpha = 2\frac{c_{12}}{c_{11}} \tag{7}$$

Often in literature α is expressed in terms of the Poisson's ratio, ν, i.e. by the relation

$$\alpha = \frac{2\nu}{1 - \nu} \tag{8}$$

which is valid for isotropic solids.

As the parallel and perpendicular strains in a biaxial strain field are related by equation 6, makes it convenient to characterize the strain of the epilayer by introducing a new quantity: the tetragonal distortion defined as

$$\varepsilon_{Tx}* = \varepsilon_{\perp x} - \varepsilon_{\parallel x} = \frac{a_{\perp x} - a_{\parallel x}}{a_x} \tag{9}$$

where the last equality follows from equations (3).

The tetragonal distortion of strained layers causes lattice directions inclined to the surface normal to appear at a different angle with respect to the corresponding direction in the undistorted lattice. The angular deviation $\Delta\theta$ is related to the lattice deformation through the relation

$$\Delta\theta = \frac{1}{2}\left(\frac{a_{\perp x}}{a_{\parallel x}} - 1\right)\sin 2\theta \tag{10}$$

where θ is the angle of the considered lattice direction with respect to the surface normal.

The channeling technique allows to measure directly the angular deviation $\Delta\theta$ and, as consequence of equation (10), the quantity

$$\varepsilon_{Tx} = \frac{a_{\perp x} - a_{\parallel x}}{a_{\parallel}x} = \frac{2\Delta\theta}{\sin 2\theta} \tag{11}$$

can be immediately derived. The quantities $\varepsilon_{Tx}*$ (Eq. (9)) and ε_{Tx} are proportional through the factor $a_{\parallel x}/a_x$ that differs from the unity by less than the misfit. For instance, for $Si_{1-x}Ge_x$ with $x = 20\%$, $(a_{\parallel x}/a_x - 1) \leq 8.3 \times 10^{-3}$. Because ε_{Tx} is directly determined and because its relative difference from $\varepsilon_{Tx}*$ is smaller than the experimental relative errors, in the following the definition of the tetragonal distortion will be that given by equation (11). The maximum value of the tetragonal distortion is obtained for a coherent growth $(a_{\parallel x} = a_0)$ and, by using equations (1, 3, 11) it is given by

$$\varepsilon_{Tx}^M = (1 + \alpha)f \tag{12}$$

In the case of DCXD, through the recording of rocking curves for symmetric and asymmetric reflections, it is possible to measure the so called mismatches, defined as the relative difference of the perpendicular and parallel lattice parameters of the layer with respect to that of the substrate

$$m_{\perp} = \frac{a_{\perp x} - a_0}{a_0} \tag{13a}$$

$$m_{\parallel} = \frac{a_{\parallel x} - a_0}{a_0} \tag{13b}$$

For a coherent growth the parallel mismatch vanishes, while for a completely relaxed layer both mismatches are equal to the misfit (Eq. (1)).

The tetragonal distortion can be derived by the difference of the perpendicular and the parallel mismatch

$$m_\perp - m_\parallel = \frac{a_{\perp x} - a_{\parallel x}}{a_0} = \frac{a_x}{a_0}\varepsilon_{Tx}* = \frac{a_{\parallel x}}{a_0}\varepsilon_{Tx} \tag{14}$$

For coherent structures this definition is identical with that given in equation (11) and in any case the relative differences between the definitions of equations (9, 11, 14) are smaller than the misfit.

In the case of Cross-section Transmission Electron Microscopy (XTEM), the thinning of the sample may introduce a relaxation in the direction normal to the cross-section plane which, for [100] cross-sections, we define as x_1. The other two axes, x_2 and x_3, lie in the cross-section plane and are parallel to the interface and perpendicular to the original wafer surface, respectively.

In this case the solution of the equilibrium equations for the elastic system is far from being straightforward. A rough approximation may be obtained by requiring that the stress tensor is still diagonal and its components are independent of x_2 and x_1. Of course the condition $\varepsilon_1 = \varepsilon_2$ (valid for an infinite interface) must be dropped. Equation (2) and the free surface boundary condition give now:

$$c_{12}\varepsilon_1 + c_{12}\varepsilon_2 + c_{11}\varepsilon_3 = 0 \tag{15}$$

By requiring that ε_2 is the same as in the biaxial case and looking for a solution which minimizes the total elastic energy of the system we obtain

$$\varepsilon_3 = \varepsilon_1 = -\varepsilon_2\frac{c_{12}}{c_{11} + c_{12}} = -\varepsilon_2\frac{\alpha}{2+\alpha} \tag{16}$$

so that the maximum tetragonal distortion becomes now

$$\varepsilon_{Tx}^{th} = \frac{a_{3x} - a_{2x}}{a_{2x}} = \frac{a_{3x} - a_0}{a_0} = f\frac{2(1+\alpha)}{2+\alpha} \tag{17}$$

where the apex th refers to thin samples (relaxation in the x_1 direction). The comparison of equations (12) and (17) shows that in the bulk case the tetragonal distortion is higher by the factor

$$R = \frac{2+\alpha}{2} = \frac{\varepsilon_{Tx}^M}{\varepsilon_{Tx}^{th}} \tag{18}$$

as compared to the thin sample case. For Si, which is the case we are dealing with, $R = 1.385$.

The above discussion is based on the assumption that ε does not depend on the coordinate along the thinning direction and as a consequence it is possible to demonstrate that the condition $a_{1x} = a_{3x}$ is realized at the interface and that ε does not depend on x_3 as well. Actually a bending of the planes perpendicular to x_1 along the x_3 direction is observed. This is an indication that the strain tensor contains also non-diagonal terms and exhibits a dependence on both x_3 and x_1. However corrections to the uniform field solution (Eq. (16)) is expected to be negligible apart from a limited region close to the film boundaries.

4. Rutherford backscattering spectrometry and channeling analysis.

4.1 EXPERIMENTAL. — The nominal composition and thickness of the layers was checked by RBS. The spectra were recorded by using a 2.0 MeV ^{4}He$^+$ beam at the Laboratori Nazionali di Legnaro (Padova). The scattering angle was chosen equal to 120° to have a good thickness resolution. The RBS measurements were calibrated in solid angle against Ta/Si standard samples whose

absolute Ta content is known with an accuracy better than 2% [7]. The beam charge collection was performed by using the whole scattering chamber as a Faraday cup reaching an accuracy better than 1%.

A high precision goniometric sample holder was used to perform the channeling analysis. Three rotation axes allow complete freedom of orientation of the sample with respect to the beam. Two linear translations allow the beam spot position to be changed on the sample surface in order to minimize radiation damage accumulation while keeping the analyzed point at the intersection of the three rotation axes. All the movements are operated by independent and fully computer controlled stepping motors. In particular one step corresponds to 0.01° for each of the rotation axes and the repeatability and the overall precision are both 0.01°.

4.2 RESULTS AND DISCUSSION.

4.2.1 *Composition determination.* — The chemical composition of the sample can be measured from the relative height of the RBS signal corresponding to the different elements. In our data reduction the experimental spectrum is simulated by a computer code through the use of trial concentration profiles until agreement with the experimental spectrum, within the statistics, is reached. As the RBS simulation program does not take into account any channeling effect, care was taken to avoid any such effect in the measure. To this purpose the random spectrum was accumulated while the sample was tilted 5° from the [001] axis and azymuthally rotated. Taking into account the symmetry of the crystal, the sample was rotated of 45° in steps of 0.5° beginning from the (110) planar channeling condition until the (100) plane was reached. At each angular step the same amount of charge was collected and the final spectrum thus resulted in an average of each angular position.

An example of the results of this measurement and analysis procedure is shown in figure 1, where the experimental and simulated spectra of the sample #4 are compared. The Ge molar fraction, x, was determined by looking at the agreement of the relative yield of Ge and Si in the alloy layer. In this way any systematic error in the stopping power function is nearly completely compensated. As a matter of fact, in this analysis any error in the stopping power enters only through the different energy of the ions in the outgoing path after scattering from Ge or from Si. As any change in the Ge molar fraction, x, produces height changes of the Si and Ge signals in opposite directions, the precision in the determination of x results to be quite good and of the order of 0.3 at %.

On the other hand, taking into account that the detection solid angle is accurately measured from the yield of the standard calibration sample, the absolute value of the stopping power influences the relative height of the simulated to the experimental spectrum and the determination of the layer thickness. In our case the Ge stopping power does not strongly influence the height of the spectrum because of its relatively low concentration ($x < 0.20$). On the contrary the Si stopping power is important for the comparison of the computed to the experimental spectrum of the Si cap , buffer layer and substrate. A good agreement was found by using the Santry and Werner [8] experimental stopping power values instead of the more used Ziegler tabulation [9]. As it is shown in figure 1 the agreement with the Si spectrum is within 1%, i.e. much better than the combined precision of the charge collection and standard sample calibration.

In figure 1 it appears that the signals of the SiGe alloy layer are rather flat and both interfaces are sharp at the RBS depth resolution limit. These facts mean that the Ge molar fraction is uniform in depth with abrupt interfaces. The same behaviour has been found for all the analysed samples except for sample #1 which shows a small and smooth increase of the Ge concentration from the buffer-alloy (b-a) interface to the alloy-cap (a-c) interface.

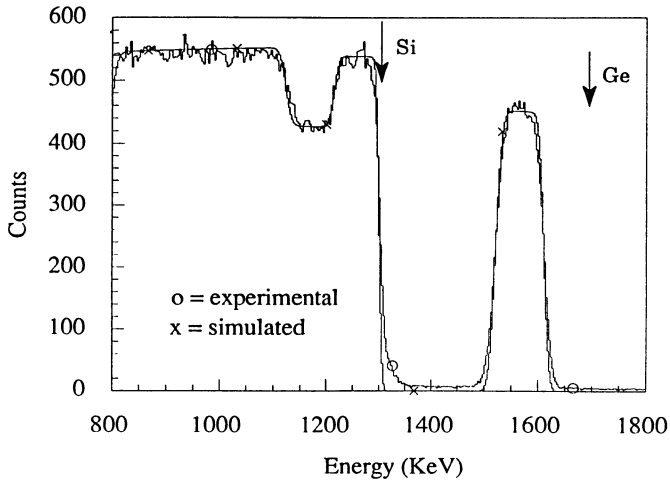The values of the Ge molar fraction for the different samples are reported in table II and com-

Fig. 1. — Experimental and computer simulated random RBS spectra for the sample #4. The arrows show the surface backscattering energy of Si and Ge. The computer simulation does not take in account the Si and Ge isotopes.

pared with the results of the other techniques used in this work. In the case of sample #1 the reported RBS value is the depth averaged value and the error bar includes the non-uniformity of the layer.

Table II. — Ge *molar fractions* (x%) *measured by the three techniques and their average values.*

Sample	Nominal	EDS	x% DCXD	RBS	MEAN
#1	0.10	7.7 ± 0.4	8.0 ± 0.3	7.7 ± 0.5	7.8 ± 0.3
#2	0.15	12.4 ± 0.4	13.1 ± 0.6	12.7 ± 0.3	12.7 ± 0.4
#3	0.20	16.0 ± 0.4	15.7 ± 0.4	15.6 ± 0.3	15.8 ± 0.3
#4	0.20	16.4 ± 0.4	16.6 ± 0.4	16.5 ± 0.3	16.5 ± 0.3

The thickness of the cap and alloy layers are reported in table III together with the results obtained by DCXD and TEM analysis. The precision of the RBS values in table III is better than the depth resolution of the technique and is obtained by the accurate calibration of the experiment (energy and solid angle) and by the use of the computer program for the simulation of the experimental spectra. The analysed volume for these measurements is of the order of 10^6 μm^3.

4.2.2 *Channeling analysis.* — A first analysis of the crystalline quality of the sample has been performed by recording the [001] axial and the (110) and ($1\bar{1}0$) planar channeling spectra. Typical results are shown in figure 2 for sample #3. The planar channeling directions have been chosen because they are particularly sensitive to the presence of misfit dislocation and selective with respect to their directions [10]. By looking at figure 2 it appears that the planar yield is characterized

Table III. — *Thicknesses of the cap and of the alloy layer determined by the three techniques.*

Sample	Nominal		DCXD		TEM		RBS	
	t_{cap}	t_{film}	t_{cap}	t_{film}	t_{cap}	t_{film}	t_{cap}	t_{film}
#1	5	100	4.1 ± 0.2	107.0 ± 0.6	4 ± 0.4	105 ± 3	4 ± 4	106 ± 3
#2	100	100	98.0 ± 0.3	99.4 ± 0.2	101 ± 3	101 ± 3	98 ± 5	100 ± 3
#3	5	100	7.6 ± 0.3	108.7 ± 0.1	8 ± 0.4	108 ± 3	8 ± 5	116 ± 3
#4	100	100	103.8 ± 0.5	104.4 ± 0.1	98 ± 3	100 ± 3	106 ± 5	106 ± 3

by many oscillations and this fact indicates a very good lattice quality of the sample. Moreover, the comparison of the dechanneling curves to the corresponding ones of a pure silicon sample indicates that the normalized yield is the same at any depth. The absence of any definite step in the yield at the interface between the SiGe alloy layer and the Si-buffer layer suggests that misfit dislocations are absent or below the sensitivity limit of the technique (about 1×10^4 lines/cm) [11].
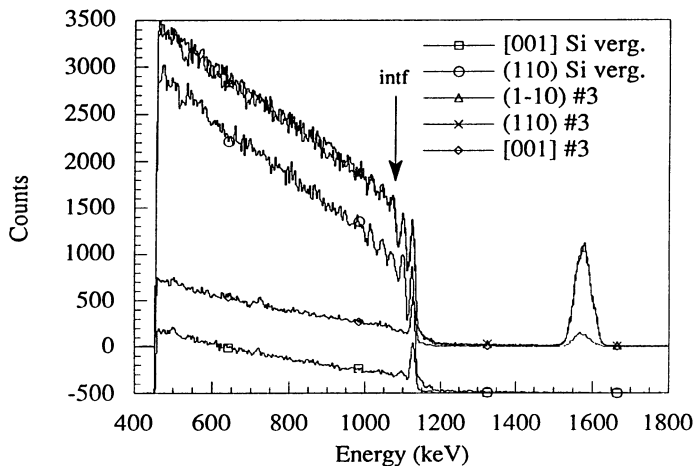

Fig. 2. — Comparison between the $<001>$, (110) and $(1\bar{1}0)$ channeling spectra of the sample #3 and the $<001>$ and (110) spectra of virgin Si. 500 counts have been subtracted from the Si vergin spectra in order to make them distinguishable from the SiGe samples. The arrow indicates the b-a interface where the dechanneling rate should increase if dislocations were present.

The Ge signal does not show the usual channeling surface peak feature because of the Si cap layer. Moreover, the channeled fraction measured respectively from the Ge and Si signals is equal, i.e. Si and Ge occupy equivalent lattice sites. This fact confirms the information about the good lattice quality of the alloy.

This type of investigation has been performed on all the samples obtaining the same results. In particular in the case of the samples with 100 nm Si cap it appears that also the a-c interface is dislocation free.

4.2.3 *Strain measurements.* — The method used to determine the lattice distortion by the chan-
neling technique is based on a high-precision measure of the absolute angular position of many
axial and planar channeling minima [12]. The value of $a_{\perp x}/a_{\|x}$ derives from a least square fitting
of all the measured channeling minima. This procedure allows the tetragonal distortion to be
determined following equation (11).

Before discussing the channeling strain measurements of our samples, we must consider the
channeling steering effect produced by the presence of the Si cap on the alloy film. In a layered
structure characterized by different strain values for each layer, a channel corresponding to an
inclined lattice direction shows a "kink" at each interface. The ideal results is that the channeling
dips of the different layers should be shifted from each other by the kink angle. However, the
planar and axial continuum potentials are able to steer part of the ion trajectories channeled in
the upper layer into the channel of the underling layer in such a way that the dips are shifted by
an angle lower than the kink angle and that their shape is no more symmetrical [13]. This effect
is very difficult to be quantitatively described, as it depends on the ratio of the layer thickness to
the oscillation wavelength of the ion trajectories in the channel [14] and on the ratio of the axial
or planar critical angle to the kink angle [15]. This is the reason why a precise measurement of
the tetragonal distortion by the channeling technique is possible only for the topmost layer of
a structure and only if reference to the substrate is not required, as in the case of the absolute
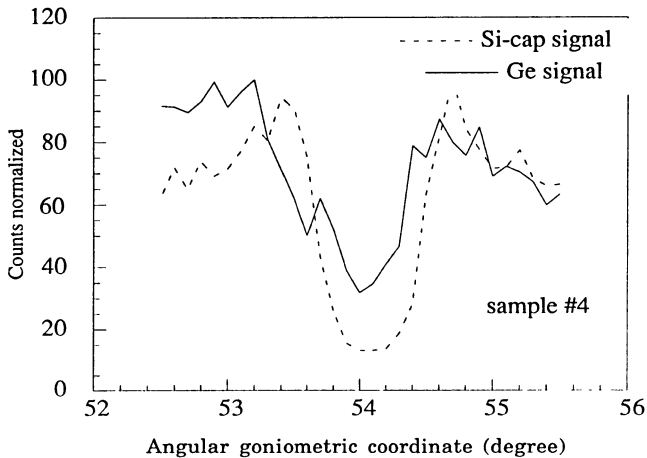angular measurements developed in our laboratory [12].

Fig. 3. — [111] dip is of the Si cap (dot-dashed line) and of the alloy layer (continuous line) for sample #4.

As an evidence of the steering effect, we present in figure 3 the [111] dips corresponding to
the Si cap layer and to the SiGe alloy layer for sample #4 having a 100 nm Si cap layer. The Ge
signal shows an asymmetrical dip with a double minimum feature. The deeper minimum roughly
corresponds to the angular position of the channeling dip of the Si cap layer, while the position
of the second minimum would correspond to a parallel strain of the alloy layer greater than the
misfit, which is clearly impossible. On the contrary, in the case of the 5 nm thick cap layer the
channeling dips of the alloy layer indicate a tetragonal distortion systematically lower than that
measured by both DCXD and CBED (see Tab. IV).

All these facts indicate that by this technique it is possible to measure only the strain of the

Table IV. — *Measured values of the tetragonal distortion for the four analyzed samples:* ε_{Tc} *is the tetragonal distortion of the cap layer measured by channeling;* ε_{Tx}^{RBS} *is the computed value of the alloy tetragonal distortion as determined by RBS-channeling (see text);* ε_{Tx}^{DCXD} *is the alloy tetragonal distortions measured by the DCXD;* $R\varepsilon_{Tx}^{CBED}$ *is the alloy tetragonal distortions measured by the CBED techniques multiplied by the ratio R to compare with the bulk case (see text);* $f(1 + \alpha)$ *is the maximum expected tetragonal distortion of the alloy layer for coherent structures.*

Sample	ε_{Tc} (%)	ε_{Tx}^{RBS} (%)	ε_{Tx}^{DCXD} (%)	$R\varepsilon_{Tx}^{CBED}$ (%)	$f(1 + \alpha)$ (%)
#1	$- - - - -$	$(0.46 + 0.06)*$	0.54 ± 0.02	0.6 ± 0.1	0.56 ± 0.02
#2	-0.015 ± 0.05	0.85 ± 0.055	0.87 ± 0.04	0.9 ± 0.2	0.89 ± 0.02
#3	$- - - - -$	$(0.96 \pm 0.04)*$	1.05 ± 0.03	1.1 ± 0.2	1.08 ± 0.02
#4	-0.03 ± 0.04	1.06 ± 0.045	1.11 ± 0.03	1.3 ± 0.2	1.12 ± 0.02

(*) These values are those measured without taking into account the channeling steering effect.

topmost layer, i.e. in our case that of the Si cap layer. However, the RBS signal of the cap layer is resolved from the Si signal of the SiGe layer only for the 100 nm thick caps and this analysis will thus be limited to samples #2 and #4. For these reasons the analysed volume for this technique is of the order of $10^5 \ \mu m^3$.

We must then find a relation between the tetragonal distortion of the cap layer and that of the underlying alloy layer. If the b-a interface is coherent, the alloy lattice parameter parallel to the interface, $a_{\parallel x}$, is equal to that of the buffer layer, a_0, and thus the Si cap layer grows without any misfit and, as a consequence, with zero tetragonal distortion. On the contrary, if the b-a interface is not coherent, let n_1 be the dislocation density at the b-a interface. The alloy parallel lattice parameter is then given by

$$a_{\parallel x} = a_0 \left(1 + b_{\parallel} \ n_1\right) \tag{19}$$

where $b_{\parallel}$ is the component of Burgers vector effective for the strain release. Of course the value of $a_{\parallel x}$ varies from a_0 ($n_1 = 0$, coherent interface) to a_x (total relaxation). In the latter situation the dislocation density is maximum and of the order of 10^5 lines cm^{-1}. In fact for 60° misfit dislocations $b_{\parallel}$ is about 0.2 nm. As the dislocation density at the b-a interface increases from zero to the maximum value, the absolute value of the tensile parallel mismatch between the cap and the alloy layer increases from zero to the maximum value corresponding to the relaxed alloy. We must then consider that also the a-c interface can be incoherent. If n_2 is the dislocation density at the a-c interface, the equivalent of equation (19) is now

$$a_{\parallel c} = a_{\parallel x} \left(1 - b_{\parallel} \ n_2\right) \tag{20}$$

where $a_{\parallel c}$ is the parallel lattice parameter of the cap layer.

By using equations (3, 6, 11) it is easy to show that the relation between the lattice parameter parallel to the interface and the tetragonal distortion of a layer is given by

$$a_{\parallel} = \frac{a(1 + \alpha)}{[(1 + \alpha) + \varepsilon_T]} \tag{21}$$

where we dropped the index x to underline its generality. So equation (19) can be rewritten as

$$\varepsilon_{Tx} = (1 + \alpha) \left[f - b_{\parallel} \ n_2(1 + f)\right] + \varepsilon_{Tc}(1 + f)(1 - b_{\parallel} \ n_2). \tag{22}$$

This equation shows that the tetragonal distortion of the alloy, ε_{Tx}, can be computed by knowing the tetragonal distortion of the cap, ε_{Tc}, and the dislocation density at the a-c interface, n_2. If the a-c interface is coherent ($n_2 = 0$) equation (22) becomes

$$\varepsilon_{Tx} = f(1 + \alpha) + \varepsilon_{Tc}(1 + f) \tag{23}$$

In our case ε_{Tc} cannot be positive (the strain of the cap can only be tensile) so that the maximum expected tetragonal distortion of the alloy is always given by equation (12). This will be realized for a perfectly coherent structure, i.e. if the coherency is realized both at the b-a and at a-c interfaces. In this case, in fact, the cap layer, having the same lattice parameter as that of the buffer layer, will not be strained and $\varepsilon_{Tc} = 0$.

Table IV reports the maximum expected tetragonal distortion of the alloy, $f(1 + \alpha)$, together with the measured ε_{Tc} for the samples with 100 nm thick cap-layer. Although the ε_{Tc} values are slightly negative, within the error bar of the measurement they are zero, indicating a perfect coherence of the whole structure.

In order to derive the tetragonal distortion of the alloy layer, we need some assumption on the dislocation density at the a-c interface. Within the sensitivity of the dechanneling technique, the previous dechanneling analysis (see Sect. 4.2.2) allows the presence of dislocations to be excluded at both interfaces. Moreover, there is another reason to exclude the presence of dislocations at the a-c interface. The misfit between the cap and the actual parallel lattice parameter of the alloy is lower than the alloy-buffer misfit unless the alloy is fully relaxed. This would require a dislocation density at the b-a interface in excess of 2×10^5 cm^{-1} which would be clearly detected by the dechanneling analysis.

Thus ε_{Tx} was deduced from equation (23) in the hypothesis of a coherent a-c interface. These values are reported in the fourth column of table IV and are compared with the results of the other techniques. Moreover, the comparison with the ε_{Tx} values to the maximum expected tetragonal distortion shows that, within the experimental uncertainties, the two values are coincident and thus the whole structure is coherent. This results was confirmed by TEM observation (see next Sect.).

In this comparison the determination of the misfit, f, is of fundamental importance. The values used in table IV are those derived from the measured Ge composition and from the lattice parameters determined by Dismukes et al. [16] as a function of the composition. These values are lower than those derived by the Vegard's law. For instance at $x = 0.20$ the relative difference amounts to 9%.

5. Analytical electron microscopy.

5.1 EXPERIMENTAL. — TEM [100] cross sections of the various heterostructures were prepared according to two different procedures of mechanical polishing, after the cutting and glueing steps which lead to the sandwich formation [17]. The first procedure involves a mechanical lapping down to 20 μm [17], whereas in the second the sandwich is dimpled down to about 10 μm. In both cases, the specimens are subsequently ion-beam milled down to perforation. The cross-sections were preferred to the corresponding plan sections also for the X-ray microanalysis. In fact, in this case the contribution to the analyzed volume from the silicon substrate, which would affect the determination in a rather unpredictable way, can be easily avoided.

The cross-sections were investigated by using a Philips CM 30 TEM, equipped with an EDAX PV9900 Energy Dispersive Spectrometer (EDS). The accelerating voltage was 300 kV for imaging and X-ray analysis purposes, and 100 kV for the Convergent Beam Electron Diffraction (CBED)

experiments. A Gatan liquid-nitrogen cooled double tilt holder was employed. The spot size at the specimen level was 10 nm, obtained in the nanoprobe mode; this mode of operation is particularly advantageous in EDS analyses, because it minimizes the contribution to the X-ray signal coming from the electrons backscattered from the lower pole pieces of the objective lens. The analyzed volume is of the order of 10^{-3} μm^3.

5.2 RESULTS AND DISCUSSION.

5.2.1 *Morphology and structure.* — A typical cross-sectional image of a Si-Ge heterostructure (sample #2) is reported in figure 4. In addition to the Si-Ge film, also the adjacent cap and buffer layers are clearly visible. The b-a interface is evidenced by the presence of small defects, which are believed to consist of oxide or carbide particles due to the contamination of the original surface of the wafer [18]. On the other hand, the b-a interface is rather smooth and free of visible lattice defects (e.g. dislocations); therefore it is a coherent interface in agreement with the channeling analysis (Sect. 4.2.3). From figure 4 the thickness of the cap, the Si-Ge alloy and buffer layers results to be 101 ± 3, 101 ± 3 and 100 ± 10 nm, respectively, in agreement with the nominal values (see Tab. I). The values of the cap and alloy thickness for all the investigated samples are reported in table III, together with the corresponding ones deduced from the other techniques.
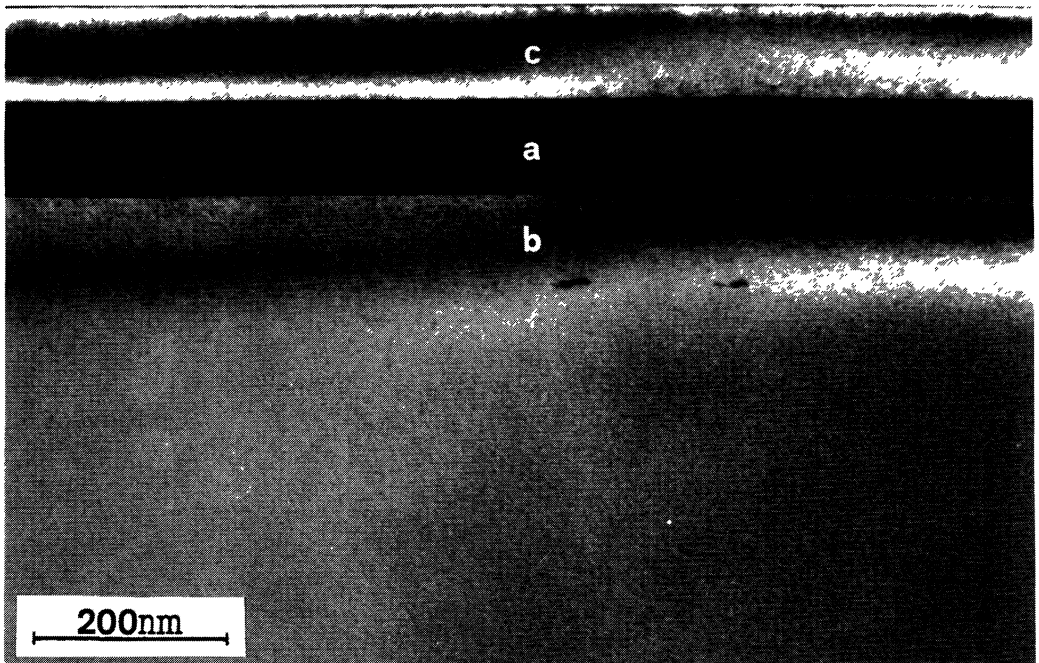

Fig. 4. — XTEM image of #2 film. The cap (c) and alloy (a) layers are clearly visible, whereas the buffer layer (b) can be detected from the small defects at the buffer/substrate interface.

5.2.2 *X-ray microanalysis.* — The film composition has been determined by TEM/EDS at 300 kV in the nanoprobe mode. The choice of the maximum accelerating voltage available in our microscope is dictated by the increase in the peak-to-background ratio and the corresponding decrease,

with increasing beam energy, of the beam broadening, thus improving the analytical accuracy and spatial resolution.

To obtain the Ge concentration in the various Si-Ge films, a previously reported analytical method has been employed [19, 20]. Basically, it consists of the intensity measurement of the SiKα and GeKα X-ray peaks generated in the Si-Ge film at two different tilt angles (0° and 20°). This method, which allows one to obtain simultaneously the composition and thickness of a thin film, requires the experimental determination of the intensity ratio, $R_m = I(SiK\alpha)/I(GeK\alpha)$ at the two tilt angles and makes use of two computer programs. The first code, named CARLONE, is a Monte Carlo simulation based on the single scattering approach and the continuous slowing down approximation. It generates two sets of computed ratios $R_c = I(SiK\alpha)/I(GeK\alpha)$ for the two tilt angles, as a function of the Ge concentration, x, and mass thickness ρt [$\mu g/cm^2$]. A procedure similar to the one proposed by Kyser and Murata [21] enables one to determine the x and ρt values which minimize the difference $|R_c(x, \rho t) - R_m|$ for the two tilt angles. Such a method, codified in the second program ROSIN, does not need standard samples for reference, provided the X-ray absorption in the berillium window of the detector is known.

In figure 5 the result of the minimization procedure in the case of sample #1 is reported both for a thin and a thick area of the sample. The experimental intensity ratios R_m were 7.97±0.08 and 8.13 ± 0.08 for 0° and 20° of tilt, respectively, in the thin area; in the thick area the corresponding values were 7.52 ± 0.08 and 7.94 ± 0.08, respectively. The crossover of the curves, corresponding to the two tilt angles, gives the Ge concentration and the local thickness of the cross section. Although this latter parameter is of no practical importance (the relevant thickness being that of the original Si-Ge film, which is immediately deduced from the width of the corresponding stripe in the cross-sectional image), the existence of a crossover in plots like the ones in figure 5 is not *a priori* predictable and is therefore a test of the quality of the experimental measurements. Moreover, the very good agreement between the concentration values found in the two regions of different thickness (compare Figs. 5a and b) indicates that the experimental X-ray intensities were free from spurious signals and that the parameters employed in the simulations were properly chosen. By considering the errors in the beam repositioning when tilting from one angle to the other and back, as well as the statistical uncertainties, an overall experimental error smaller than 2% can be estimated. The effect of this error on the final result is evaluated by the bootstrap statistical method discussed in detail in reference [19]. The experimental errors are found to exert a very small influence on the accuracy of the concentration determination, though the error in the thickness value is somewhat larger. For instance, assuming for the experimental errors the above figure of 2% and including 1000 bootstrap replications in the calculation, the estimated accuracy of the concentration is better than 1%, while that of the mass thickness is of 5% and 3%, for the thin and the thick area, respectively. This is agreement with the results obtained by the bootstrap method in the case of the $TiSi_x$ films [20], the larger error in the thickness determination being due to the small difference in X-ray path (and hence in absorption) between the 0° and 20° geometries, particularly in thin areas. In any case, as pointed out above, the local mass thickness of the TEM cross section is of no interest in this context. The data on the Ge concentration in the investigated Si-Ge films are summarized in table II and compared to those derived by RBS and DCXD.

5.2.3 *Convergent beam electron diffraction.* — The lattice strain of the Si-Ge films has been measured through changes in the position of High Order Laue Zone (HOLZ) lines within the central disc of CBED patterns. These patterns have been performed at 100 kV in a <130> projection. This low acceleration voltage was chosen because it is well known that the visibility of HOLZ lines degrades by increasing the electron beam energy [22].

The experimental patterns were taken at the liquid-nitrogen temperature and compared to the
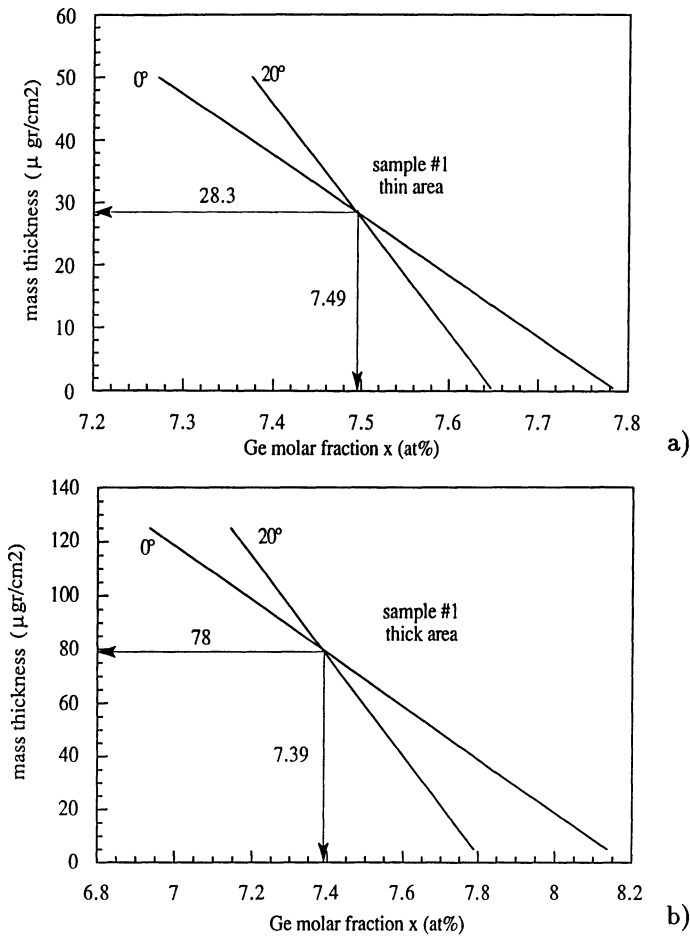
Fig. 5. — Germanium concentration *vs.* the local mass thickness ρt in two different areas of the #1 film in a TEM cross section like the one in figure 4. The two pairs of curves correspond to the X-ray spectra taken at the two tilting angles (0° and 20°, respectively) in a thin (a) and a thick (b) region of the sample.

ones simulated by a computer programme by Stadelmann [23], based on the kinematical approximation. First, the effective accelerating voltage V_0 was determined by taking a CBED pattern on a region of the substrate (i.e. perfect silicon) and varying this parameter in the simulation until the best match with the most prominent experimental HOLZ lines was obtained. In the calculations, the silicon lattice parameter $a_0 = 0.54288$ nm, which is the value corresponding to the sample temperature of 100 K, was employed.

Likewise, assuming the transferability of the V_0 value from the silicon substrate to the strained layers, the lattice parameter of the various Si-Ge films in the different directions was determined. This method has been extensively discussed by Lin *et al.* [24] and Bithell and Stobbs [25]. These authors have shown that the above kinematical approximation is valid when comparing materials with differences in mean atomic number smaller than about 5 units. In our case the transferability assumption should hold, as the maximum difference in mean atomic number (i.e. between sample #4 and Si) is about 3.

As for the tetragonal distortion, we have already noted in section 3 the difference between the bulk case, which holds for the DCXD and RBS experiments, and the one of the TEM cross sections where, due to the thinning of the sample, a relaxation in the direction normal to the cross-section plane occurs. As already asserted, if there are no dislocations, there is no relaxation along the x_2 direction in which the sample size can be considered as infinite; hence $a_{2x} = a_0 = 0.54288$ nm. However, it may occur in practice that in the TEM sample the condition under which equation (16) has been derived is not realized, so that the cell of the SiGe alloy becomes slightly orthorhombic $(a_{1x} \leq a_{3x})$ [26]. Consequently the ratio R is slightly lesser than that reported in equation (18).

In any case, the values of the cell parameters a_{1x} and a_{3x} are deduced from a comparison between experimental and simulated CBED patterns, as described above. From these values, the experimental tetragonal distortion ε_{Tx}^{CBED} is calculated from equation (17).

An example of agreement between the experimental and the computed CBED patterns is reported in figure 6 which refers to the sample #4. The parameters used for the matching are $a_{1x} = a_{3x} = 0.5477$ nm and, of course, $a_{2x} = a_0 = 0.5429$ nm; therefore, in this case a tetragonal distortion was able to reproduce the experimental CBED pattern. In some other cases this was not strictly verified. For instance in the case of sample 2 a_{1x} resulted to be 0.5463 nm and $a_{3x} = 0.5465$ nm. Anyway, the deviation from perfect tetragonality is quite small, so it was assumed that $a_{1x} = a_{3x}$ throughout this work. The values of ε_{Tx}^{CBED}, obtained with the above described procedure, are then converted into bulk-equivalent values through the R factor (Eq. (18)). These values are reported in table IV and compared to those deduced from DCXD and RBS measurements.

6. Double crystal X-ray diffraction.

6.1 DCXD PROCEDURES. — The X-ray rocking curves (RCs) were obtained by a double-crystal diffractometer (DCXD) arranged in $(n, -n)$ parallel configuration for 004 symmetric and 224 asymmetric reflections with Cu Kα_1 wavelength. The analysed volume for DCXD is of the order of 5×10^6 μm^3. The use of these two types of reflections was necessary to determine the depth profiles of the perpendicular and parallel components of the lattice mismatch between alloy and substrate (Eqs. (13)) and hence the coherent or incoherent nature of the b-a interface. The intensity values were recorded with a single channel analyzer regulated in order to avoid any contribution of the λ/n harmonics to the counting rate. The degree of reliability of the intensity values and the angular positioning of the samples was verified by obtaining perfect matching between experimental and calculated RCs of a high quality [001] silicon crystal aligned according to the 004 symmetric and 224 grazing incidence, asymmetric reflections [27].

Since different parameters (alloy thickness, Ge atomic fraction, lattice mismatch depth-gradient and static Debye-Waller factor) influence the intensities diffracted from the alloy, in order to discriminate among their effects, the X-ray reflectivities have to be controlled experimentally very carefully. This was made by checking the stability of the source over a period of time much longer than that necessary for recording a single measurement and by the precise determination of the dead time of the counting apparatus.

The experimental RCs of the samples were simulated by using the dynamical model of diffraction reported by Wie et al. [28] and the minimization procedure adopted in a previous work [29]. Modifications to this model were used because the diffraction parameters of the alloy, different from those of pure silicon, were found effective for a precise RC simulation. The changes, whose influence was previously discussed [30], are the following:

(i) The real and imaginary parts of the atomic scattering factors, including the temperature
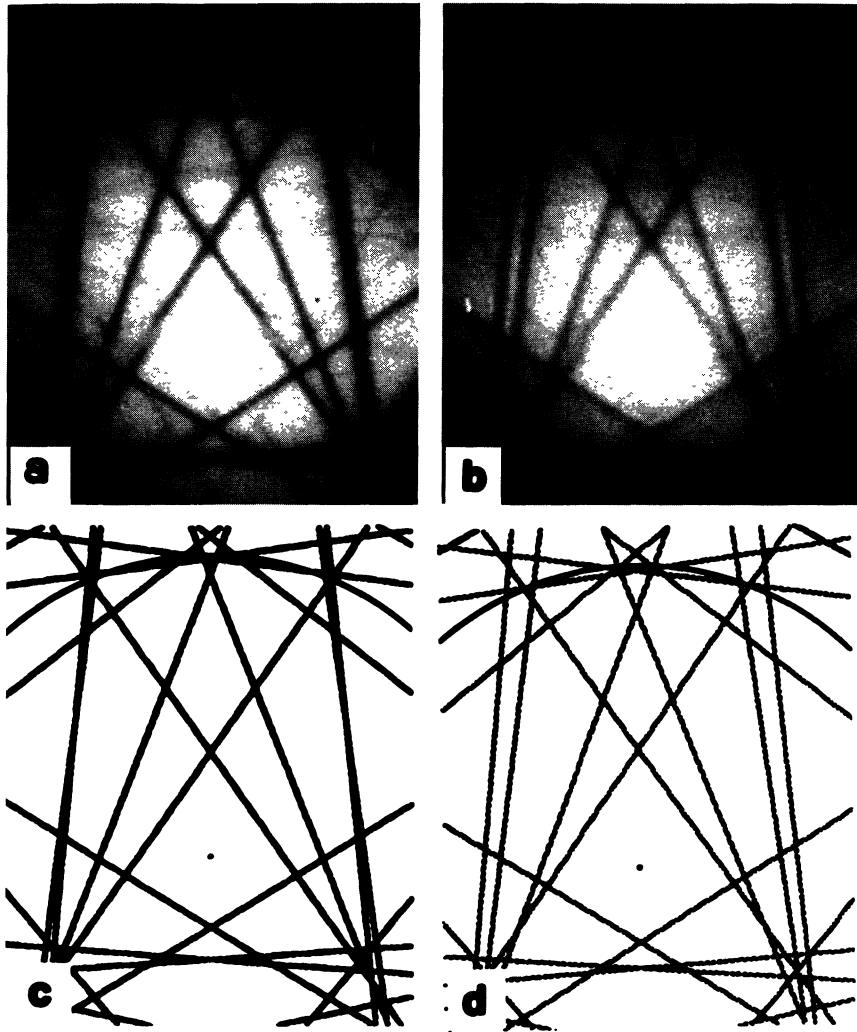
Fig. 6. — Experimental (a,b) and computed (c,d) CBED patterns, taken on the silicon substrate (a,c) and on thin Si-Ge alloy of sample #1 film (b,d). <001> cross section,<130> projection.

factors and the dispersion corrections, are linearly averaged over the solute concentration (x). This expression is justified by the fact that the nominal Ge fractions involved here are in the range $0.1 \le x \le 0.2$, i.e. they are sufficient to give an appreciable contribution to the total diffracted intensity. In fact, the Ge scattering factor is about three times greater than that of Si at the values of $\sin \theta_B / \lambda$ corresponding to the 004 and 224 spectra (here θ_B is the kinematical Bragg angle).

(ii) The volume of the unit cell of the solid solution, which appears in the expression of the crystal polarizability per unit volume (the fundamental parameter in X-ray diffraction), varies according to $m_\perp$ and $m_\parallel$.

(iii) The kinematical Bragg angle of the alloy is modified according to x, because of the increase of the lattice parameter given by substitutional Ge.

iv) The usual expression describing the departure of the Bragg angle of the alloy from that of

the silicon substrate

$$\Delta\theta_B = -\left[\left(m_\perp \cos^2\gamma + m_\parallel \sin^2\gamma\right)\tan\theta_B + \left(m_\perp - m_\parallel\right)\sin\gamma\cos\gamma\right] \quad (24)$$

where $m_\perp$ and $m_\parallel$ were defined in equation (13) and γ is the angle between surface and diffracting planes, is valid as a first approximation for sufficiently small mismatch values. Hence, it was replaced by the second order expression [27]

$$\Delta\theta_B = \frac{1 - \sqrt{1 + 2\left[\left(m_\perp - m_\perp^2\right)\cos^2\gamma + \left(m_\parallel - m_\parallel^2\right)\sin^2\gamma\right]\tan\theta_B + \left(m_\perp - m_\parallel\right)\sin 2\theta_B \tan\theta_B}}{\tan\theta_B} \quad (25)$$

The angle γ between surface and diffracting planes corresponding to the nominal crystallographic orientation was measured by a Seifert MZ VI diffractometer equipped with an Eulerian cradle and was kept as a fixed parameter in the simulation program. All these items must be taken into account in order to avoid differences between the mismatch profiles obtained by simulating the symmetric and asymmetric RCs of the same sample [27]. Moreover, as the dynamical model used [28] calculates only the diffracted intensity as a function of the angular setting of the sample, the thermal and Compton diffuse intensities, scattered from a thick, perfect Si crystal outside its range of total-reflection, were measured and taken into account, following the method previously described [29].

The variable parameters used by the computer in an iterative program for the simulations of the 004 symmetric and 224 asymmetric RCs, were the depth profiles of $m_\perp$ and $m_\parallel$ between alloy layer and substrate, the thicknesses of the cap, of the alloy and of the buffer layers. In a step of the interaction, the program calculates the Ge atomic fraction x and all the quantities that depends on it using as input quantities the previously determined values of $m_\perp$ and $m_\parallel$. The program stops when the sum over all the experimental points of the squares of the difference between calculated and observed intensities is less than 10^{-4}. The calculus procedure is the following. The components $m_\perp$ and $m_\parallel$ are related to the misfit parameter f according to

$$f = \frac{m_\perp + \alpha\, m_\parallel}{1 + \alpha} \quad (26)$$

Moreover, if the misfit parameter is assumed to be linear with x in a not too wide range of composition, we have

$$f = \beta\, N\, x \quad (27)$$

where β is the expansion coefficient and N the silicon atomic density. The β coefficient was determined from the X-ray analysis of silicon wafers implanted with Ge ions [30]. The ratio between the integral of the lattice mismatch depth profile and the implanted dose gave $\beta = (7.53 \pm 0.03) \times 10^{-25}$ cm^{3}at^{-1}. This value is lower than that foreseen by the Vegard's law $\left(8.34 \times 10^{-25}\ \text{cm}^3\text{at}^{-1}\right)$ and coincides with the one reported by Dismukes et al. [16]. The x data, obtained from the above equations, and the static Debye-Waller factor related to the mean square displacement of the atoms from the lattice sites, reproduce the X-ray intensities diffracted from the solid solutions. This allows one to simulate correctly the RC tails of the samples.

6.2 DCXD - RESULTS AND DISCUSSION. — Figure 7 is the comparison between experimental and simulated symmetric RCs of the sample #4. The agreement is quite good over all the angular range, where the satellite peak is produced by diffraction from the alloy film and the intensity
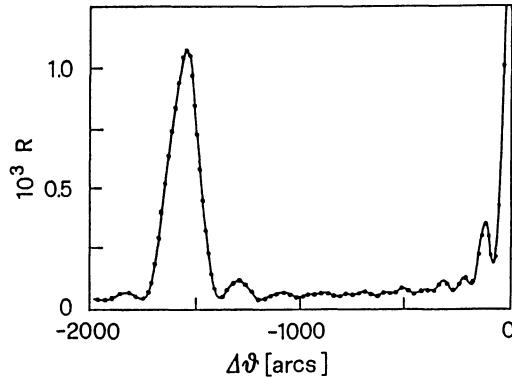
Fig. 7. — Experimental (dots) and simulated (continuous line) 004 RCs of #4 sample. $\Delta\theta = 0$ individuates the diffraction position of the silicon substrate, corrected for the refractive index.
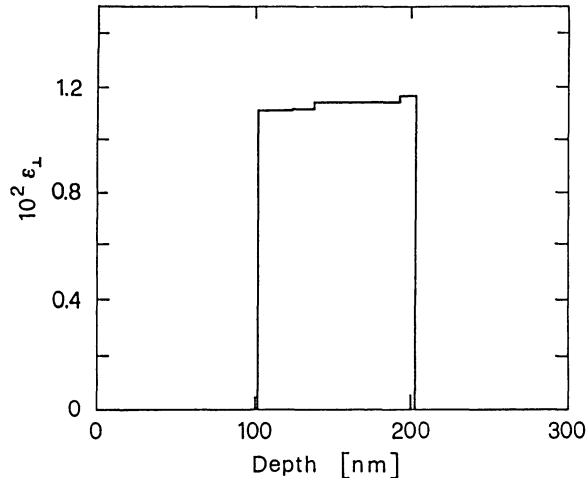

Fig. 8. — Perpendicular mismatch profile resulting from figure 7.

oscillations are related to the thickness of the cap and the Si-Ge film. The profile of the perpendicular lattice mismatch, resulting from the RC simulation, is shown in figure 8 and differs from a rectangular box. However, as the gradient is small and the absorption in the thin surface layer is low, it is impossible to determine the actual sign of the gradient.

Figure 9 shows the comparison of the experimental 224 grazing incidence and emergence asymmetric RCs with those calculated for sample #4. The calculation was performed by using the same perpendicular mismatch distribution as that of the 004 RC (Fig. 8b). The matching between experiment and calculation was made possible by the use of the second-order expression in item (iv) equation (25) and by taking into account the deviation angle of the (001) lattice planes from the wafer surface. This indicates that plastic relaxation did not occur at the b-a interface, which agrees with the fact that for $x = 0.166$ the alloy thickness of 100 nm is smaller than the critical one for the onset of misfit dislocations [31, 32]. Due to the absence of misfit dislocations $\left(m_{\parallel} = 0\right)$ in the most concentrated alloy, and hence *a fortiori* in the other samples, the perpendicular mismatch $m_{\perp}$ co-
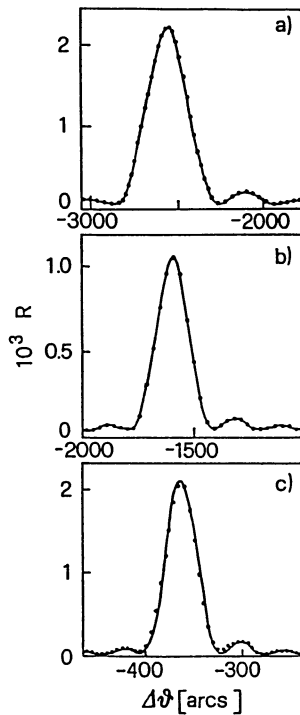
Fig. 9. — Simulation of the 004 satellite peak of the #4 sample (b) and calculation of the 224 grazing incidence (a) and emergence (c) asymmetric RCs by using the perpendicular mismatch profile relative to (b).

incides with the expected maximum tetragonal distortion ε_{Tx}^M. The results of the X-ray analyses of all four samples are shown in tables II to IV. It is worth noting that the values of the perpendicular mismatch were obtained by RC simulation and not by direct reading of the angular separation between substrate and layer peaks, because the latter procedure leads to significant errors mainly for very thin surface layers [33]. The lattices of the Si cap and buffer layers resulted to be undeformed. Therefore, the buffer thicknesses were not reported, as their perfection makes them indistinguishable from the unperturbed substrates.

The tetragonal distortions (Tab. IV) and the consequent Ge atomic fractions (Tab. II) are averaged over the layer thicknesses and the uncertainties reported in table II correspond to the standard deviations of x which resulted to be larger than the errors associated with both the β coefficient and the ε_{Tx} measurements.

7. Discussion and conclusions.

Four $Si_x Ge_{1-x}$ layers epitaxially grown by MBE on Si [001] substrates at different values of the Ge molar fraction have been analysed by AEM, DCXD and RBS-channeling. The structural analyses have shown that all the samples have high lattice quality and that there are no dislocations. As a consequence these samples represent a good test bench for comparing the performances of the three techniques for the analysis of strained heterostructures in absence of lattice defects. In general, from the comparison of the results reported in tables II to IV, it is possible to conclude

that the analytical results show a quite good overall agreement. In the following we try to conclude about the best performances of each technique.

i) Tetragonal distortion. From the data of table IV it appears that the results of the DCXD technique are affected by the lowest errors. The RBS-channeling technique, while having no significantly higher errors (independently of the presence of dislocations), is limited to the topmost layer of the sample [12]. However, in the present case by the measurement of the tetragonal distortion of the cap (when its thickness is large enough) and taking into account that there are no dislocation at the c-a interface the tetragonal distortion of the film could be derived with the same precision. On the other hand, the CBED technique, when performed on cross sections, allows one to obtain local information on the tetragonal distortion of the Si-Ge alloy. The values of tetragonal distortion found by this method are smaller than the actual ones, due to the relaxation induced by the thinning process; however, the values corresponding to the bulk case can be easily deduced, with a fair accuracy. Moreover, the inherent high spatial resolution makes it possible to perform strain determinations also in dislocated specimens, by simply focusing the beam outside the defective region. From all these facts we can conclude that the DCXD technique is the best one to measure the lattice strain in samples without dislocations.

ii) Alloy composition. The data of table II not only show an excellent agreement among the results of the employed techniques, but also indicate comparable errors. However, it must be stressed that only the EDS and RBS techniques allow a composition measurement independent of the strain measure. Moreover, the EDS technique on thin cross sectioned samples allows a very good depth resolution, because the concentration profile can be determined by analyzing areas in the image plane as small as 10 nm in diameter; on the other hand, the depth resolution of RBS makes it the best technique for unthinned samples.

iii) Layer thickness. The relatively good precision of the RBS technique requires a careful energy calibration and the use of a computer code for the simulation of the spectra. The results of DCXD come from the reproduction of the intensity oscillations between layer and substrate peak in the RC. The error associated with this measurement is closely related to that of the angular positioning of the sample. This was measured over an angular range of approximately one degree and resulted to be less than 0.1%. The errors reported for DCXD in table III, though very small, are larger than 0.1% and represent the standard deviations from the mean value obtained from several measurements made on different points of each sample. This fact also implies a very good lateral homogeneity of the samples. Here again the results of DCXD are not independent of the strain measurements. X-ray experiments indicate that the interface roughness, if any, is negligible; this is confirmed by TEM observations. The TEM technique allows the measurement not only of the cap and the alloy film, but also of the buffer layer thickness, through the detection of small defects and/or contaminations at the substrate interface. Finally DCXD has the best precision and accuracy in thickness measurement of the alloy film even if it can not determine the buffer thickness that can be well measured by TEM.

The overall agreement of the results of the different techniques indicates that systematic errors can be reasonably excluded and this fact allows a few additional considerations. The systematic difference in the nominal values of composition an thickness from the measured values in tables I and II derives from the calibration technique employed during MBE growth. Typically the growth rates are individually calibrated by the deposition of thick amorphous films, whose thickness is used to calibrate the fluxes. We have observed that this measurement, while quick and simple, yields a systematically lower Ge concentrations consistent with the measurements in table II. The differences are due to a lower density of the amorphous deposited Ge used for calibration.

The thickness values derived from RBS are systematically influenced by the value of the used stopping powers. From our results it appears that the Si stopping power measured by Santry and Werner [8] bears consistent results while the commonly used Ziegler [9] tabulation would lead to

thickness values systematically lower by 6.6%. On the contrary, we cannot say anything about the Ge stopping power because its relative weight is less than 25%.

As to the EDS analysis, the main systematic errors come from the choice of the ionization cross sections and the absorption of X-rays in the berillium window of the detector, whose thickness is not accurately known. For this reason an accuracy of 5% is in general assumed for thin film analysis using K-lines. However, the overall agreement of the Ge concentration values among the three techniques, reported in table II, indicates that for the silicon-germanium pair a better accuracy is obtainable.

More relevant from a physical point of view is the comparison of the measured strain values with the expected ones. For the CBED experiments, the errors associated with the ε_{Tx} values stem from the precision of the lattice parameter determination, which in turn depends on the matching between experimental and computed patterns. An error smaller than 4×10^{-4} is found in our measurements. However, it seems that the values of the tetragonal distortion deduced by CBED are systematically higher than those found by DXCD and RBS (Tab. IV). The reason for this is probably due to the complex relaxation of the cross-sectioned samples, which is not accounted for with sufficient accuracy by the simple formulas used here.

Of some relevance in the DCXD technique could be the systematic errors coming from the error in the dead time of the counting chain (the measured errors of 2% gives reflectivity errors of about 0.7% in the RC region of the layer peak) and from the neglecting of the sample curvature (about 0.01 m^{-1} in the sample with the highest x value). However, these errors involve minor uncertainties in the values reported in tables II to IV.

In addition to the very good lattice quality of the samples, it is possible to give also high assurance to the growth technique as regards the thickness, whose nominal values are in agreement with the experimental determination. On the contrary, the nominal molar fractions are higher than the measured values of about 19%. From the strain release process point of view, we can maintain that the critical thickness at which dislocations begin to nucleate at the substrate-alloy interface is greater than 100 nm for the samples with at least 16% of Ge molar fraction. On the other hand, the absence of dislocations and the measurement of the lattice strain are consistent in the framework of the tetragonal elastic distortion only taking into account the deviation from the Vegard law.

References

[1] PATTON G.L., IYER S.S., DELAGE S.L., TIWARI S. and STORK J.M.C., *IEEE-ED Lett.* **9** (1988) 165.
[2] PATTON G.L., COMFORT J.H., MEYERSON B.S., CRABBE E.F., SCILLA G.J., de FRESART E., STORK J.M.C., SUN J.Y.C., HARAME D.L. and BURGHARTZ J.N., *IEEE-ED Lett.* **11** (1990) 171.
[3] KASPER E., KIBBEL H. and KOENIG U., *Mat. Res. Soc. Symp. Proc.* **220** (1991).
[4] IYER S.S., Chapter 2 in Epitaxial Silicon Technology, B.J. Baliga Ed. (Academic Press, Orlando FL, 1986).
[5] IYER S.S., TSANG J.C., COPEL M.W., PUKITE P.R. and TROMP R.M., *Appl. Phys. Lett.* **54** (1988) 219.
[6] LANDAU L.D. and LIFSHITZ E.M., Theory of Elasticity (Pergamon Press, New York, 1959).
[7] COHEN C., DAVIS J.A., DRIGO A.V. and JACKMAN T.E., *Nucl. Instrum. Meth.* **218** (1983) 147.
[8] SANTRY D.C. and WERNER R.D., *Nucl. Instrum. Meth.* **178** (1978) 523.

[9] ZIEGLER J.F., Stopping Power and Ranges of Ions in Matter (Pergamon Press, New York, 1977, Vol. n. 4).

[10] ROMANATO F., DRIGO A.V., MAZZER M., *Nucl. Instrum. Meth.* **B63** (1992) 36.

[11] MAZZER M., CARNERA A., DRIGO A.V., FERRARI C., *J. Appl. Phys.* **68** (1990) 531.

[12] CARNERA A. and DRIGO A.V., *Nucl. Instrum. Meth.* **B44** (1990) 357.

[13] BERTI M., CARNERA A., DRIGO A.V., GENOVA F., PAPUZZA C. and RIGO C., *E-MRS Symp. Proc.* **6** (1986) 227.

[14] PICRAUX S.T., CHU W.X., ALLIEN W.R., ELLISON J.A., *Nucl. Instrum. Meth.* **B15** (1986) 306.

[15] HASHIMOTO S., FENG Y.Q., GIBSON W.B., SHOWALTER L.J. and HUNT B.D., *Nucl. Instrum. Meth.* **B13** (1986) 45 (Proc. 11th Int. Conf. Atomic Collision in Solids).

[16] DISMUKES J.P., EKSTROM L., PAFF R.J., *J. Phys. Chem.* **68** (1964) 3021.

[17] GARULLI A., ARMIGLIATO A. and VANZI M., *J. Microsc. Spectrosc. Electron.* **10** (1985) 135.

[18] OTTEN M., *Philips Bull.* **127** (1989) 3.

[19] ROSA R. and ARMIGLIATO A., *X-ray Spectrom.* **18** (1989) 19.

[20] ARMIGLIATO A. and ROSA R., *Ultramicroscopy* **32** (1990) 127.

[21] KYSER D.F. and MURATA K., *IBM J. Res. Dev.* **18** (1974) 352.

[22] FRASER H.L., LORETTO M.H. and EADES J.A., in: Intermediate voltage microscopy and its application to materials science (Ed. K. Rajan) (Electron Optics Publishing Group, Philips Electronic Instruments, Inc., Mahwah N.J., 1987) p. 17.

[23] STADELMANN P., *Ultramicroscopy* **21** (1987) 131.

[24] LIN Y.P., PRESTON A.R., VINCENT R., *Institute of Physics Conf. Ser.* I.o.P. Publ., Bristol, **90** (1987) 115.

[25] BITHELL E.G. and STOBBS W.M., *J. Microsc.* **153** (1989) 39.

[26] MAHER D.M., FRASER H.L., HUMPHREYS C.J., KNOLL R.V. and BEAN J.C., *Appl. Phys. Lett.* **50** (1987) 574.

[27] SERVIDORI M., CEMBALI F., FABBRI R. and ZANI A., *J. Appl. Cryst.* **25** (1992) 46.

[28] WIE C.R., TOMBRELLO T.A. and VREELAND T. Jr, *J. Appl. Phys.* **59** (1986) 3743.

[29] SERVIDORI M. and CEMBALI F., *J. Appl. Cryst.* **21** (1988) 176.

[30] CEMBALI F., FABBRI R., SERVIDORI M. and ZANI A., *Mat. Res. Soc. Symp. Proc.* **208** (1991) 225.

[31] BEAN J.C., FELDMAN L.C., FIORY A.T., NAKAHARA S. and ROBINSON I.K., *J. Vac. Sci. Technol.* **A2** (1984) 436.

[32] KOHAMA Y., FUKUDA Y. and SEKI M., *Appl. Phys. Lett.* **52** (1988) 380.

[33] FEWSTER P.F. and CURLING C.J., *J. Appl. Cryst.* **62** (1987) 4154.